Improving hexahedral-FEM-based plasticity in surgery simulation

Ruiliang Gao and Jörg Peters

University of Florida, Gainesville, FL32611, USA

Abstract. Collecting, stretching and tearing soft tissue is common in surgery. These repeated deformations have a plastic component that surgeons take into consideration and that surgical simulation should model. Organs and tissues can often be modeled as curved cylinders or planes, offset orthogonally to form thick shells. A pair of primary directions, e.g., axial and radial for cylinders, then provides a quadrilateral mesh whose offset naturally yields a hexahedral mesh.
To better capture tissue plasticity for such hexahedral meshes, this work compares to and extends existing volumetric finite element models of plasticity. Specifically, we extend the open source simulation framework SOFA in the context of surgical simulation. Based on factored deformation gradients, the extension focuses on the challenge of separating symmetric and asymmetric, elastic and plastic deformation components – while preserving volume and avoiding re-meshing.

Keywords: laparoscopic simulation, soft tissue, real-time simulation, SOFA, elastoplasticity

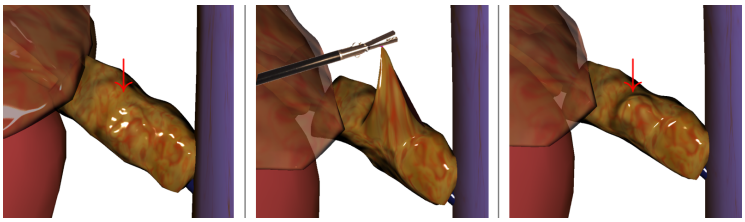

Fig. 1: Laparoscopic surgery simulation: stretching fatty tissue. Note the vestigial plastic deformation at ↓

1 Motivation

Tearing internal soft tissue is, besides cutting and cauterizing, an important surgical skill – to mobilize vessels and organs held in place by connective and

fatty tissue. Realistic tearing requires a plastic deformation of the tissue – that is the tissue does not spring back to its initial position when released.

When surgeons interact with virtual tissues in a real-time training environment, perfect shape memory in the form of perfect elasticity is distracting and some plastic deformation is expected as thick tissues or organ walls stretch. Plastic deformation should also be monitored to penalize over-stretching.

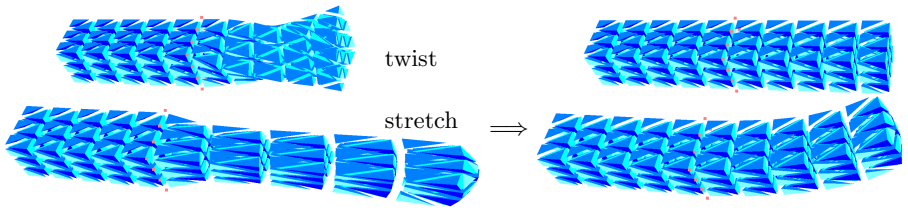

(a) initial twist/stretch (b) final deformation

Fig. 2: SOFA tet-element plasticity: (*top*) twist, (*bottom*) stretch. (a) initial deformation (b) (*top*) lack of plasticity, (*bottom*) lack of symmetry.

To improve real-time simulation of soft tissue undergoing plastic deformation for training, we build on an existing simulation platform, the Simulation Open Framework Architecture (SOFA). SOFA [1] offers plastic deformations albeit currently only for linear tetrahedral elements. It however efficient and natural to generate meshes for surgical simulation as an offset from a quadrilateral base surface. Fatty tissue can often be presented as an offset of a covering surface sheet Fig. 3b. Thick-walled organs of the gastrointestinal tract have a natural tube structure (and so does the covering tissue, recall Fig. 1). Other organs can be embedded into a hexahedral free-from deformation grid as illustrated in Fig. 3a. Offsetting a quadrilateral mesh yields a hex-mesh, e.g., a partition of a tissue into boxes that is predictable and immediate. When splitting the natural hexahedra into tetrahedra to apply SOFA's plasticity code, we experienced unnatural stiffness Fig. 2, *top*; and asymmetry when choosing an asymmetrical tetrahedralization Fig. 2, *bottom*. We noted also that algorithmically generated tetrahedral partitions can change strongly for small changes the enclosing surface and so lack the symmetry and feature alignment of hex elements.

Currently no *hex*-FEM codes exist that model plasticity in an interactive environment for surgery simulation. This paper reports on an extension of SOFA to allow for plastic deformations of hex-elements. The extension represents a careful trade-off between higher accuracy and simplicity of computation via a 'blended-vertex approach'. The contributions are as follows.

- Extending the linear co-rotational elasto-plastic FEM to hex meshes.
- Extending the third-order accurate blended-vertex deformation [2] to hex meshes. (The increased degrees of freedom enables coarse hex meshes to replace high-resolution tet meshes when modelling large plastic deformations).

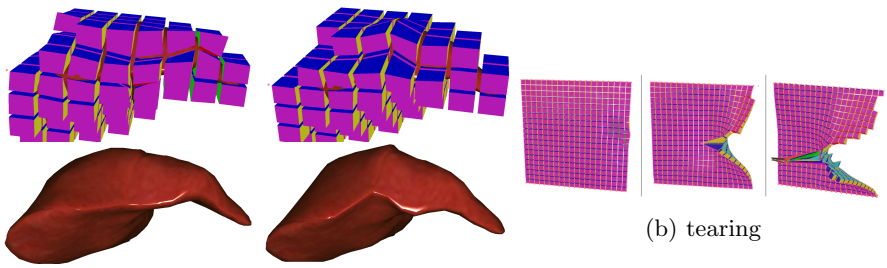

(a) plastic bending and stretching

(b) tearing

Fig. 3: Interactive surgical models (a) Piecewise hexahedral free-form deformation cage enclosing the liver. (b) Tearing a peritoneal sheet.

- Devising a simple plastic decomposition scheme that handles both rotational and stretching plasticity.
- Implementing and comparing the blended vertex approach and the cell-centered piecewise constant approach to plastic rotational deformation. 4 rotational deformation both vertex-centered (The blended vertex approach is more flexible and accurate, the cell-centered approach yields better element quality.)
- Preserving volume over large deformations.

2 Background

The choice of tetrahedral vs hexahedral finite elements to model elasticity has been debated for many years in the context of engineering analysis. [3,4] observe that contact pressure distribution and contact shear stress distribution predicted by linear tetrahedral mesh are noisy and mesh dependent resulting in patches of locally elevated peak pressures whereas the pressure distribution predicted on hexahedral (and quadratic tetrahedral) meshes was smooth and uniform. More recently [5] argued that total degree quadratic finite elements on tetrahedra provide comparable outcomes to tri-linear elements on hexahedra. The authors later make the case for adding non-polynomial polyhedral elements [6].

In practice, for real-time soft tissue simulation, both tri-linear elements on hex-partitions and linear (total degree) tetrahedral elements are commonly used. Unsurprisingly, compared with linear tetrahedral elements, tri-linear hex elements are more flexible, perform better over viscous regions and have higher accuracy [7,8]. SOFA offers both hex and tet elements. Tessellating organs like the liver into tetrahedra is well automated (e.g., [9]) whereas quick and reliable coarse hex-meshing remains a challenge that has spawned an active research community, see e.g., [10,11,12,13]. Luckily, simulated organs and tissues can often be outlined as curved cylinders or planes, that are offset orthogonally to form thick shells: A pair of primary directions, e.g., axial and radial for cylinders, provides a quadrilateral mesh whose offset naturally yields a regular hexahedral

mesh. The flexibility of hex-elements compared to linear tet elements comes at a cost: preservation of volume is tricky, but necessary in surgery simulation so that plastically deformed tissue neither artificially swells nor disappears.

The material point method (MPM, [14,15,16]) need not be concerned with distortion of mesh elements, a major concern for the FEM approach. MPM excels at modelling plasticity of granular materials like sand or snow. However such materials are not typically relevant to surgical simulation. SPH-type approaches do not take advantage of the available regular quad-offset structure. The well-known linear elastic co-rotational FEM [17] factors out rotational components (the displacement is treated as $\mathbf{R}\hat{\mathbf{x}} - \mathbf{x}$ in the notation developed in the next Section, where $\mathbf{R}$ describes the material rotation). Co-rotational FEM therefore models primarily stretching in a major direction.

3 Methodology

Plastic deformation occurs when a material is subjected to tensile, compressive, bending, or torsion stresses that exceed the material's yield strength. With $\mathbf{x}$ the start position, possibly plastically deformed in a previous iteration, and $\hat{\mathbf{x}}$ the deformed position in world coordinates, displacement is infintesimally characterized by the Gradient $\hat{\mathbf{J}} := [\frac{\partial \hat{\mathbf{x}}_i}{\partial \mathbf{s}_j}]$, where $\mathbf{s}$ are the domain (reference) coordinates. The relative gradient, called deformation gradient,

$$\mathbf{F} := \frac{\partial \hat{\mathbf{x}}}{\partial \mathbf{x}} = \frac{\partial \hat{\mathbf{x}}}{\partial \mathbf{s}} \frac{\partial \mathbf{s}}{\partial \mathbf{x}} = \frac{\partial \hat{\mathbf{x}}}{\partial \mathbf{s}} (\frac{\partial \mathbf{x}}{\partial \mathbf{s}})^{-1} = \hat{\mathbf{J}}(\mathbf{J})^{-1} \tag{1}$$

of a deformed hex element with vertices $\mathbf{v}^i$ can be measured at the center point $\mathbf{o} := \sum_i \mathbf{v}^i/2^3$ and called $\mathbf{F_o}$ – or at one of the vertices i and named $\mathbf{F}_i$. [2] proposes to increase accuracy by blending for hex k and vertex i the gradients as $\overline{\mathbf{F}}_i^k := (\mathbf{F}_i^k + \mathbf{F}_\mathbf{o}^k)/2$.

Plasticity decomposition. Recent approaches [18,19,20] recommend multiplicative decomposition of the deformation gradient into elastic and plastic parts: $\mathbf{F} = \mathbf{F}^e\mathbf{F}^p$ both for better numerical stability, to support compressibility and because the classic additive (strain) decomposition $\epsilon = \epsilon^e + \epsilon^p$ is only accurate for infinitesimal strains but fails for large deformations (or to easily model incompressibility). Starting with the singular value decomposition $\mathbf{F} = \mathbf{UDV}^T$ where $\mathbf{D}$ is the diagonal and $\mathbf{U}, \mathbf{V}$ are orthogonal (rotations or reflections), the total deformation is factored into a (polar, orthogonal) rotation tensor $\mathbf{R}$ and a symmetric positive-definite tensor called the (right) stretch tensor $\mathbf{S}$:

$$\mathbf{F} = (\mathbf{UV}^T)(\mathbf{VDV}^T) = \mathbf{RS}. \tag{2}$$

Following [19] we determine the elastic component. Then we extract the plastic components from both the rotation and the stretch tensor to obtain the factoring

$$\mathbf{F} = \mathbf{R}^e\mathbf{R}^p\mathbf{S}^e\mathbf{S}^p \tag{3}$$

into elastic rotation, plastic rotation, elastic stretch and plastic stretch as follows.

Plastic stretching. Following [20] the linearized strain $\epsilon = \mathbf{V}(\mathbf{D} - \mathbf{I})\mathbf{V}^T$ is derived from $\mathbf{S}$ and converted into the first Piola–Kirchhoff stress σ by the classic stress-strain relation. Then the plastic stretching deformation is

$$\mathbf{S}^p = \mathbf{V}(\frac{\mathbf{D}}{(\det \mathbf{D})^{1/3}})^\gamma \mathbf{V}^T \quad \gamma := \min\{\nu \Delta t \frac{\|\sigma\|_2 - \tau}{\|\sigma\|_2}, 1\} \tag{4}$$

for a plastic flow rate ν, plastic yield threshold τ and time step Δt.

Plastic rotation. Separating the plastic rotation from the rotation tensor is a challenging problem [21], because the material rotation stems from two sources: shape changing deformation, e.g., shear deformation, and rigid body rotations. When the material changing shape, it is typically not possible to uniquely separate out the rigid body rotation. However, in our surgical simulation context there is no spinning anatomy and we can neglect angular velocity or inertia-related factors. We can therefore assume that plastic rotation depends solely on rotational distortion. We measure rotational distortion as the magnitude of the angle based on geodesics on the unit sphere defined as [22]

$$\Phi(\mathbf{R}_1, \mathbf{R}_2) := \| \log(\mathbf{R}_1 \mathbf{R}_2^T) \| \in [0, \pi]$$

and apply this measure to the rotational component obtained from polar decomposition at the center $\mathbf{F_o} = \mathbf{R_o U_o}$, respectively blended, $\overline{\mathbf{F}}_i^k = \overline{\mathbf{R}}_i^k \overline{\mathbf{U}}_i^k$. For vertex i and the center $\mathbf{o}$ of hex k this yields the decomposition of the blended vertex rotation $\overline{\mathbf{R}}_i^k$ of (2) so that, dropping the superscript k, and denoting the identity matrix as $\mathbf{I}_3$,

$$\begin{aligned} \overline{\mathbf{R}}_i^e \, \overline{\mathbf{R}}_i^p &:= \overline{\mathbf{R}}_i^{(1-\eta)} \, \overline{\mathbf{R}}_i^\eta = \overline{\mathbf{R}}_i, \\ \eta &:= \nu^R \Delta t (\phi_i^k - \tau^R)/(\phi_i^k + \Phi(\mathbf{I}_3, \mathbf{R_o})), \quad \phi_i^k := \Phi(\overline{\mathbf{R}}_i^k, \mathbf{R}_\mathbf{o}^k). \end{aligned} \tag{5}$$

for a rotation yield-threshold $\tau^R \in [0, \pi]$, rotational plastic flow rate $\nu^R \in [0, 1]$.

The above vertex plastic rotation is based on each vertex's local rotation. This yields flexibility and accuracy but potentially allows strong distortion. Alternatively we propose cell-centered decomposition of rotation to determine a centered rigid rotation $\mathbf{R}_\mathbf{o}^p$ that largely preserves the hexahadral element's shape.

$$\begin{aligned} \mathbf{R}_\mathbf{o}^p \mathbf{R}_\mathbf{o}^e &= \mathbf{R}_\mathbf{o}^{\tilde{\eta}} \mathbf{R}_\mathbf{o}^{1-\tilde{\eta}}, \\ \tilde{\eta} &:= \nu^R \Delta t (\tilde{\phi}^k - \tau^R)/(\tilde{\phi}^k + \Phi(\mathbf{I}_3, \mathbf{R_o})), \quad \tilde{\phi}^k = \max_{i \in \text{hex}^k} \phi_i^k. \end{aligned} \tag{6}$$

Material hardening. To implement the material hardening, we update the plastic yield threshold by $\tau \leftarrow \tau + \kappa\gamma\|\sigma\|$ and the rotation yield threshold by $\tau^R \leftarrow \tau^R + \kappa\eta\phi_i^k$. The parameter κ controls the amount of work hardening (or softening) per time step.

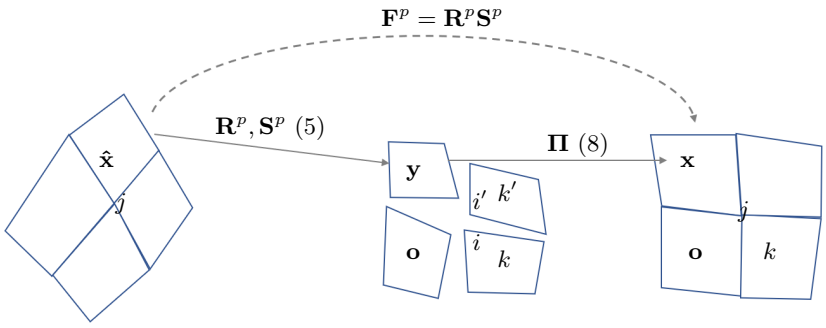

Fig. 4: Representation of a quad-mesh (analogous to a hex-mesh) in (*left*) elastically deformed world space (where the surgery takes place), (*middle*) rest space (isolated elements with strongly deformed domains) and (*right*) material space (relaxation of the deformations to a consistent mesh). The dashed path is not used for iteration.

Plastic update. At each time step, the plastic stretch $\mathbf{S}_i^p$ first updates the rest position of each vertex i of an isolated rest space element k (see Fig. 4,*middle*):

$$\mathbf{y}_i^k \leftarrow \mathbf{y}_i^k + \mathbf{S}_i^p \mathbf{u}_i, \quad \mathbf{u}_i := \mathbf{R}_i \hat{\mathbf{x}}_i - \mathbf{x}_i, \tag{7}$$

where $\mathbf{u}_\alpha$ is the co-rotational vertex displacement [17]. For vertex plastic rotation, we update the rotation map (see Fig. 4)

$$\mathbf{\Pi}_i^k \leftarrow \mathbf{\Pi}_i^k \overline{\mathbf{R}}_i^p, \tag{8}$$

and for the alternative cell-center plastic rotation $\mathbf{\Pi}^k \leftarrow \mathbf{\Pi}^k\ \mathbf{R}_\mathbf{o}^p$.

Even though constructions (4) and (5) imply $\det(\mathbf{S}_i^p) = \det(\mathbf{R}_i^p) = 1$, the volume of each element is not locally preserved, because the plastic offset is applied separately per vertex. Computing the exact volume from the Jacobian $\mathbf{J}$, the ratio β of the deformed volume divided by the original volume can be accurately computed. For element k we update $\mathbf{y}_i^k$ by scaling back to the initial volume:

$$\mathbf{y}_i^k \leftarrow \mathbf{y}_i^k + (\mathbf{y}_i^k - \mathbf{o}^k)(1-\beta)\Delta t \tag{9}$$

where Δt distributes the the adjustment over the iterations so that short time steps animate to slower volume restitution. To combine the vertices $\mathbf{y}_i^k$ of the isolated elements and form a consistently joined 'material', we update $\mathbf{x}_j \leftarrow \sum_{k \in N_j} \mathbf{\Pi}_i^k \mathbf{y}_i^k / |N_j|$, where $\mathbf{y}_i^k$ are the $|N_j|$ vertices corresponding to the material space vertex $\mathbf{x}_j$ with global index j in the surrounding cells N_j, see Fig. 4.

4 Results and Discussion

We have incorporated our plasticity decomposition approach by extending linear hexahedral FEM in SOFA 19.12. The examples illustrate some parameter choices. All tests, see also the video, were conducted on a PC with Intel Core

i7-9700K CPU and 8G RAM running Windows 10. Our code executes at 25-33 hex/ms, For the most expensive computational time steps, immediately after release, our code is ca 20% slower than SOFA's elastic-only corotational code.

Fig. 5 compares the stretching of a 9×10-hex bar under different plasticity flow rates ν, plastic yield thresholds τ. The bar is clamped at the middle (shown as black dots) and the stretching force is applied at the central face on the end of the bar. Results show the distribution of the plastic deformations where cross section symmetry is preserved. (The views vary due to perspective projection).

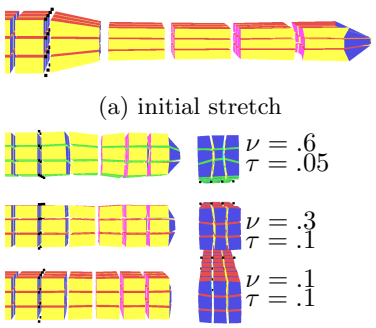

(a) initial stretch

(b) final deformation

Fig. 5: Stretching bars with *top* to *bottom*: high, medium, low stretch plasticity material. Faces between slice 5 and 6 are clamped. (a) initial stretch, (b) side and cross-section views of final deformed rest pose.

Fig. 6 juxtaposes the blended vertex plastic rotation with the cell-center plastic rotation by twisting the bar with different rotational plasticity flow rates ν^R, and rotational plastic yield thresholds τ^R. The twisting force is applied tangentially at all the four edge centers of the central face of the bar cross-section. Tests show that both

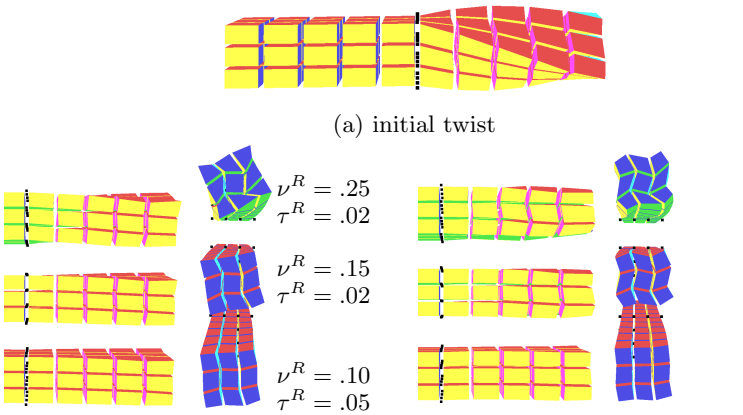

(a) initial twist

(b) blended vertex method

(c) cell-center method

Fig. 6: Twist and plasticity. *top* to *bottom*: high, medium, low rotational plasticity material. (a) initial twist, (b,c) final plastic deformation (side view, *left*; front cross-sectional view, *right*).

methods can capture plastic rotation related to the flow rate ν^R. However, the deformation differs: the vertex approach is better at preserving the cross-sectional shape but distorts each local element more than the cell-centered approach. The cell-centered approach preserves the local box shape but the cross-sectional view is jagged.

For all configurations of Fig. 5 and Fig. 6, the volume of the final deformed bars agrees with the input volume within $< 1\%$. The material hardening parameter is $\kappa = 0.2$ in all test cases. This choice proved effective in preventing ill-shaped material elements due to large plastic deformations: before an element becomes highly distorted its plastic yield threshold is reached and causes fracture.

Twist torques due to rotation of lap surgery instrument heads are extremely low [23]. As a practical solution in the surgical simulation setting, our implementation switches off plasticity when an element is about to become inverted – the remaining elastic FEM solver handles inverted elements robustly [24]. Switching to a purely elastic simulation when hexahedral elements are about to invert favors robustness over physics during flawed, unrealistic high-torque interactions.

We use plasticity for surgical training simulation for a range of anatomical features and laparoscopic surgical procedures. Fig. 3a illustrates the plastic deformation of a free-form deformation cage, a piecewise trilinear function on a coarse hexahedral mesh that transform an embedded much finer mesh. Fig. 3b illustates tearing peritoneum. See also the accompanying video.

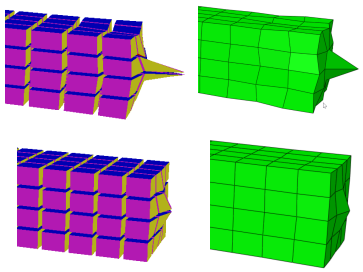

(a) Our Method (b) C3D8R

Fig. 7: FEM beam simulations using (a) our 8-node hex corotational elasto-plasticity (Young's 5000, Poisson .45), (b) Abaqus 8-node hex element (C3D8R) with hyperelasto-plasticity (Moon-Rivlin, C10=1765, C01=43, D1=1E-05). Initial Stretch, *top*; final plastic deformation, *bottom*, agree for (a) and (b).

A comparison of FEM beam simulations between our method and the Abaqus C3D8R hyperelasto-plasticity model is shown in Fig. 7. At ca 7ms per hex Abaqus analysis does not meet real-time constraints. While linear Abaqus C3D8R model stretches locally and visibly less realistic in the 'eyeball norm' of real-time simulation, Fig. 7 shows remarkable agreement on the location of highest deformation and within 5% in the stretch during temporal evolution between the sophisticated hyper-elastic model and our co-rotational extension. As tissue is better modeled as hyper-elastic material, we have no formal analysis to explain the agreement but note that the applications typically have a high Poisson ratio.

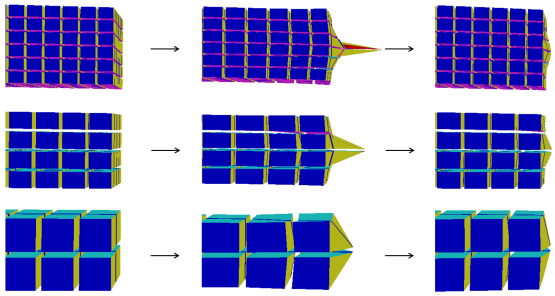

Fig. 8: Refining the stretch test. *left*: initial mesh; *middle*: maximal stretch; *right*: final plastic deformation.

Fig. 8 illustrates self-refinement. The three beam models reproduce the same deformation, localized commensurate with the higher resolution. Execution time for refinement scales linearly with the number of hex-elements since no explicit matrix is built or inverted.

Limitations While generating hex meshes by offsetting natural quad-meshes is highly efficient, the process does not easily lend itself to re-meshing when hex elements become ill-shaped. Our implementation relies on the material hardening to prevent distortion and switches to pure elasticity when elements invert.

To avoid polar rotation ambiguity, we restrict the maximal element rotation to less than π. To increase the total object's rotational angle, the initial mesh has to be designed with sufficiently many pieces (what is usually not a problem in the context of a given surgical procedure).

References

1. Faure, F., Duriez, C., Delingette, H., Allard, J., Gilles, B., Marchesseau, S., Talbot, H., Courtecuisse, H., Bousquet, G., Peterlik, I., Cotin, S.: SOFA: A Multi-Model Framework for Interactive Physical Simulation. In Payan, Y., ed.: Soft Tissue Biomechanical Modeling for Computer Assisted Surgery. Volume 11 of Studies in Mechanobiology, Tissue Engineering and Biomaterials. Springer (June 2012) 283–321
2. James, D.L.: Phong deformation: a better C^0 interpolant for embedded deformation. ACM Transactions on Graphics (TOG) **39**(4) (2020) 56–1
3. Tadepalli, S.C., Erdemir, A., Cavanagh, P.R.: Comparison of hexahedral and tetrahedral elements in finite element analysis of the foot and footwear. Journal of biomechanics **44**(12) (2011) 2337–2343
4. Benzley, S.E., Perry, E., Merkley, K., Clark, B., Sjaardama, G.: A comparison of all hexagonal and all tetrahedral finite element meshes for elastic and elasto-plastic analysis. In: Proceedings, 4th international meshing roundtable. Volume 17., Citeseer (1995) 179–191
5. Schneider, T., Hu, Y., Dumas, J., Gao, X., Panozzo, D., Zorin, D.: Decoupling simulation accuracy from mesh quality. ACM Trans. Graph **37**(6) (2018) 280:1–280:14

6. Schneider, T., Dumas, J., Gao, X., Botsch, M., Panozzo, D., Zorin, D.: Poly-spline finite-element method. ACM Trans. Graph **38**(3) (2019) 19:1–19:16
7. Shepherd, J.F., Johnson, C.R.: Hexahedral mesh generation constraints. Engineering with Computers **24**(3) (2008) 195–213
8. Sarrate Ramos, J., Ruiz-Gironés, E., Roca Navarro, F.J.: Unstructured and semi-structured hexahedral mesh generation methods. Computational Technology Reviews **10** (2014) 35–64
9. Hu, Y., Schneider, T., Wang, B., Zorin, D., Panozzo, D.: Fast tetrahedral meshing in the wild. ACM Trans. Graph **39**(4) (2020) 117
10. Blacker, T.D.: Automated conformal hexahedral meshing constraints, challenges and opportunities. Eng. Comput **17**(3) (2001) 201–210
11. Liu, H., Zhang, P., Chien, E., Solomon, J., Bommes, D.: Singularity-constrained octahedral fields for hexahedral meshing. ACM Trans. Graph **37**(4) (2018) 93:1–93:17
12. Cherchi, G., Alliez, P., Scateni, R., Lyon, M., Bommes, D.: Selective padding for polycube-based hexahedral meshing. Comput. Graph. Forum **38**(1) (2019) 580–591
13. Gao, X., Shen, H., Panozzo, D.: Feature preserving octree-based hexahedral meshing. Comput. Graph. Forum **38**(5) (2019) 135–149
14. Schreck, C., Wojtan, C.: A practical method for animating anisotropic elastoplastic materials. In: Computer Graphics Forum. Volume 39., Wiley Online Library (2020) 89–99
15. Stomakhin, A., Schroeder, C., Chai, L., Teran, J., Selle, A.: A material point method for snow simulation. ACM Transactions on Graphics (TOG) **32**(4) (2013) 1–10
16. Wang, S., Ding, M., Gast, T.F., Zhu, L., Gagniere, S., Jiang, C., Teran, J.M.: Simulation and visualization of ductile fracture with the material point method. Proceedings of the ACM on Computer Graphics and Interactive Techniques **2**(2) (2019) 1–20
17. Hauth, M., Strasser, W.: Corotational simulation of deformable solids. (2004)
18. Irving, G., Teran, J., Fedkiw, R.: Invertible finite elements for robust simulation of large deformation. In: Proceedings of the 2004 ACM SIGGRAPH/Eurographics symposium on Computer animation. (2004) 131–140
19. Bargteil, A.W., Wojtan, C., Hodgins, J.K., Turk, G.: A finite element method for animating large viscoplastic flow. ACM transactions on graphics (TOG) **26**(3) (2007) 16–es
20. Wicke, M., Ritchie, D., Klingner, B.M., Burke, S., Shewchuk, J.R., O'Brien, J.F.: Dynamic local remeshing for elastoplastic simulation. ACM Transactions on graphics (TOG) **29**(4) (2010) 1–11
21. Holmedal, B.: Spin and vorticity with vanishing rigid-body rotation during shear in continuum mechanics. Journal of the Mechanics and Physics of Solids **137** (2020) 103835
22. Huynh, D.Q.: Metrics for 3d rotations: Comparison and analysis. Journal of Mathematical Imaging and Vision **35**(2) (2009) 155–164
23. Richards, C., Rosen, J., Hannaford, B., Pellegrini, C., Sinanan, M.: Skills evaluation in minimally invasive surgery using force/torque signatures. Surgical endoscopy **14**(9) (2000) 791–798
24. Irving, G., Teran, J., Fedkiw, R.: Tetrahedral and hexahedral invertible finite elements. Graphical Models **68**(2) (2006) 66–89